Direct simulation of a directional solidification experiment observed *in situ* and real-time using X-ray imaging

Direct simulation of a directional solidification experiment observed *in situ* and real-time using X-ray imaging

G Reinhart[1,3], Ch-A Gandin[2,3], N Mangelinck-Noël[1,3], H Nguyen-Thi[1,3], B Billia[1,3], J Baruchel[4]

[1] Aix-Marseille Univ & [3] CNRS, IM2NP UMR 6242, Campus Saint-Jérôme Case 142, 13397 Marseille Cedex 20, France
[2] MINES ParisTech & [3] CNRS, CEMEF UMR 7635, 06904 Sophia Antipolis, France
[4] ESRF, Avenue des Martyrs, BP 220, 38048 Grenoble Cedex, France

E-mail: Charles-Andre.Gandin@mines-paristech.fr

Abstract. It has been shown in the last decade that *in situ* and real-time observation of metallic alloy solidification is possible by using X-ray monitoring conducted at third generation synchrotron sources. A detailed analysis of a Bridgman experiment carried out at ESRF with an Al - 3.5 wt% Ni alloy was presented earlier [1]. This article proposes a direct simulation of the solidification of the entire sample for this experiment, in which all the dendritic grains are individually represented as they nucleate and grow in the experiment. This is possible by extracting from the radiographs a list of all the nucleated grains, including the positions and orientations of their main trunks. Simulation is performed using a two-dimensional (2D) Cellular Automaton (CA) – Finite Element (FE) model. As a result of the coupling between the CA and FE methods, consequences of the macroscopic transport of heat, liquid momentum and solute mass on the development of the dendritic grain structure are accounted for, and vice versa. The macroscopic deformation of the columnar front observed during the experiment is reproduced, as well as the columnar-to-equiaxed transition. The influence of flow patterns on macrosegregation is also discussed.

1. Introduction

Solidification of metallic alloys usually starts with the nucleation of crystals. Each crystal grows and adopts a dendritic morphology to form a single grain. During its development, each grain can be identified as an envelope which contains a mixture of a primary solid phase plus an intradendritic liquid, i.e. a mixture referred to as mushy zone. The grain morphology can be more or less elongated depending on the local history of the temperature and melt composition in its neighboring. For instance, growth in a temperature gradient may result in an elongated columnar grain structure whereas a uniform temperature would favor isotropic equiaxed grain morphology. The presence of liquid flow due to buoyancy forces also influences the grain morphology and could modify the solute transport (micro- and macro-segregation). In addition, such solute transport leads to variations of the solidification conditions and then an inhomogeneous distribution of the fraction of solid phases formed upon dendritic, peritectic and eutectic microstructures between the intra and intergranular regions.

In situ and real-time direct observation of all these dynamical phenomena is now possible by using X-ray monitoring conducted at third generation synchrotron sources [2-4]. On other hand, modeling of these observations is still a challenge, mainly because it requires models including heat and mass

transfers coupled with physical phenomena taking place at various length scales. First comparisons between X-ray observations of solidification and numerical models have yet been reported [5, 6]. In the present contribution, a Bridgman experiment carried out at the European Synchrotron Radiation Facility (ESRF, Grenoble, F) with a refined Al - 3.5 wt% Ni alloy [1] is thoroughly characterized and used as a benchmark, with the goal to provide inputs for a 2D CAFE model [5]. This enables us to perform a direct simulation of the dendritic grain structure and the eutectic distribution in the entire sample accounting for fluid flow and its interaction with the growing solid microstructures. Most recent advances in coupled experimental and numerical analyses are demonstrated.

2. Experimental details

2.1. Solidification experiments at ESRF

Directional solidification experiments were performed in a Bridgman-type furnace at the ID19 imaging beamline of ESRF [7, 8]. The sample was made of an Al - 3.5 wt% Ni alloy with addition of 0.5 wt% Al-Ti-B to generate particles acting as preferred nucleation sites for new grains. Its dimensions were 40 mm in length and 6 mm in width. The thickness was reduced to 150-200 µm in order to obtain sufficient transmission of the X-ray beam. The sample was adjusted into a soft graphite crucible. Radiographs of the solidifying samples were recorded with an ESRF FReLoN (Fast Read-out Low Noise) camera in order to display the time-evolution of the microstructure. The optics was chosen to obtain a good compromise between a large field of view (15×6 mm^2) and a good spatial resolution (pixel size = 7.46 µm). X-ray beam energy was set to 13.5 keV using a double Si(111) monochromator and the acquisition frequency was about 0.3 Hz which is a compromise between satisfactory contrast and high acquisition rate.

Solidifications were performed upward, in stable conditions with respect to thermosolutal convection, with a heavy solute rejected during the solidification that increases the liquid density and a positive temperature gradient of approximately 30 $K.cm^{-1}$. For the solidification experiment that will be discussed presently, solidification started with a low pulling velocity, 1.5 $\mu m.s^{-1}$, leading to the formation a columnar dendritic structure. A permanent regime was established after approximately 4200 s. The pulling velocity was then suddenly increased to a value of 4 $\mu m.s^{-1}$ in order to activate nucleation in undercooled region above the interface and provoke a Columnar to Equiaxed Transition (CET).

2.2. Image processing and analysis

The image processing software ImageJ [9] was used in order to remove spurious artifacts on the radiographs due to the non-uniform profile of the X-ray beam, monochromator defects or surface defects on the crucible. Image processing consisted in a flat-field correction of the radiographs, and then in a division by a corrected image of the same zone recorded earlier when the alloy was fully liquid. More detail regarding this procedure can be found in [1]. The final result is an enhanced contrast and almost defect free image of the grain structure, with the Al-rich dendritic structures appearing in light grey and the Ni-rich regions such as the eutectic structure appearing in dark grey. A quantitative characterization of the solidification experiment and the final grain structure was performed in order to determine experimental parameters to be used as input, or for comparison with the numerical simulations. Because the field of view is limited to a small window, an entire image of the final grain structure was deduced by pasting partial radiographs of the sample after complete solidification (figure 1a). Segmentation of the grains was performed manually by drawing the corresponding envelopes (figure 1b). Individual grains were identified by using the particle analysis function of ImageJ. The positions of the grain nucleation centers, after sedimentation if any, were determined unambiguously from the solidification movie. The corresponding coordinates (X_i,Y_i) were defined in a reference frame placed at the bottom center of the sample as identified in figure 1b. The crystallographic orientation of the dendritic grains could not be determined during the experiment or during *post-mortem* analyses since the sample was remelted to carry out further solidification

experiments. Thus, the orientation of the longest primary arm growing upward relative to the vertical growth direction, θ_i, was measured for each grain (figure 1c). Finally, the positions of the highest dendrite tip and of the eutectic front, and therefore the mushy zone height, were measured as a function of time.

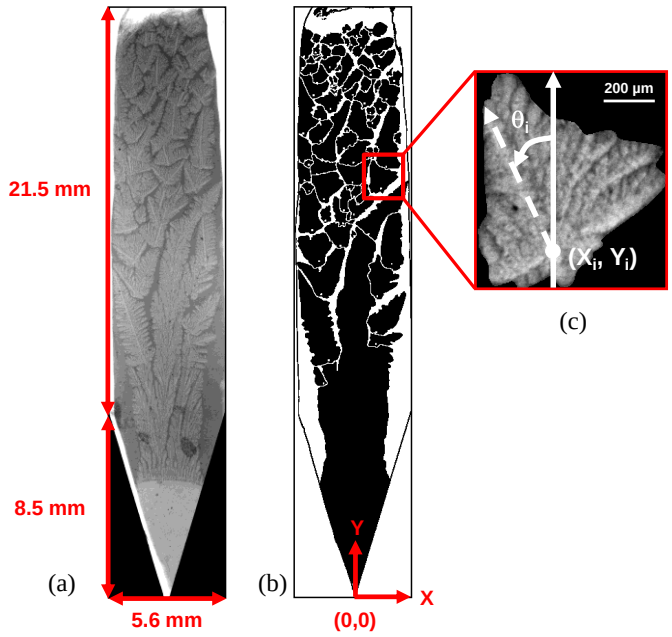

Figure 1. (a) Reconstructed image of the fully solidified sample with its characteristic dimensions used in the numerical simulations, (b) image of the grain structure after segmentation and (c) example of determination of the grain orientation and grain centre.

3. Modelling

3.1. Cellular Automaton – Finite Element modeling

A volume averaging approach is used to write conservation equations for a representative elementary volume (REV) made of a mixture of one solid phase, s, plus one liquid phase, l. No other phase being present, the sum of their volume fraction is equal to unity: $g^s + g^l = 1$. Furthermore, equal and constant densities in the phases are assumed, $\rho^s=\rho^l=\rho_0$, together with a fixed solid phase, $\mathbf{v}^s=0$. As a consequence, the average total mass conservation equation simplifies to $\nabla\cdot\langle\mathbf{v}\rangle = 0$ where the average macroscopic flow velocity reduces to $\langle\mathbf{v}\rangle = g^l \langle\mathbf{v}^l\rangle^l$, $\langle\mathbf{v}^l\rangle^l$ being the average intrinsic velocity of the liquid phase. When writing the momentum conservation over the REV, a permeability term appears that is calculated thanks to the Carman-Kozeny relationship, $[g^{l\,3}\,\lambda_2^{\,2}] / [180\,(1-g^l)^{\,2}]$, where a constant value of the secondary dendrite arm spacing, λ_2, is taken, deduced from measurements. The Boussinesq approximation is introduced: the liquid density, ρ^l, is kept constant in all terms of the momentum equation except for the gravity term where it is replaced by a function of the local solute composition in the liquid phase, $\langle w^l\rangle^l$, and the local temperature, T, $\rho^l = \rho_0 \left[1 - \beta_T\,(T - T_L) - \beta_w\,(\langle w^l\rangle^l - w_0)\right]$, where β_T and β_w denote the thermal and solutal expansion coefficients, respectively. References used to define the variations of the liquid density with the local solute composition in the liquid phase and the local temperature are the liquidus temperature of the alloy, T_L, and its nominal composition, w_0, respectively. The other physical parameter of the momentum equations is the dynamic viscosity of the liquid phase, μ^l. The average heat flow equation is also considered. The average enthalpy per unit mass, $\langle H\rangle = C_p\,T + g^l\,\Delta^l_s H_f$, is linked to the specific heat taken constant for the liquid and solid phases, $C^s_p = C^l_p = C_p$, and to the latent heat of fusion per unit mass, $\Delta^l_s H_f$. The thermal conductivities of the alloy in the solid, κ^s, and in the liquid, κ^l, (table 1) are taken constant. The variation is linear in the mushy zone between the eutectic temperature, T_E, and the liquidus temperature. Finally, the average conservation of the solute mass is written for a binary alloy with the average composition of solute, $\langle w\rangle$, as the main unknown. The physical parameter

entering in the solute mass balance is the diffusion coefficient of the solute element in the liquid phase, D^l. A more detailed presentation of the set of equations is presented elsewhere [10] as well as in this proceedings volume [11]. The main guidelines to solve these equations in a two dimensional representation with the FE method are provided elsewhere [12, 13].

A microsegregation model is needed to convert the average composition of solute, <w>, and the average enthalpy, <H>, into a temperature, T, and a fraction of solid, g^s. It is based on the coupling between a CA method to track the development of the grain envelopes and a local microsegregation model based on the lever rule approximation. The FE mesh is further divided into a regular lattice of fine squares named CA cells. Each cell is defined by its center coordinates and the finite element in which it is located. Linear interpolation coefficients are computed between the FE nodes and the CA cell, thus permitting interpolation of the variables solved by the FE method onto the CA grid. Similarly, information computed onto the CA grid can be summed up and projected onto the FE mesh. Each cell is also attributed with an index that defines its state. At the beginning of a simulation starting from a superheated melt, all cells are in the liquid state. As nucleation and growth proceed, the index of cell is changed to a non-zero value. The growth of the structure in a cell is also characterized by the size of its local mushy zone. It is defined by the extension of a square, the four apices representing the dendrite trunks and arms directions. A dendrite tip kinetics defined in [14] is used, with the Gibbs-Thomson coefficient, Γ, as the main parameter. The cell is then in a mushy state, i.e. made of a mixture of solid and liquid phases. Its fractions of phases are computed by converting the projected average enthalpy and composition at the cell position into a temperature and a fraction of solid and liquid phases assuming the lever rule approximation. Once the prescribed growth temperature of the eutectic structure is reached, a simple isothermal transformation is assumed in order to transform the remaining liquid phase into a volume fraction of eutectic.

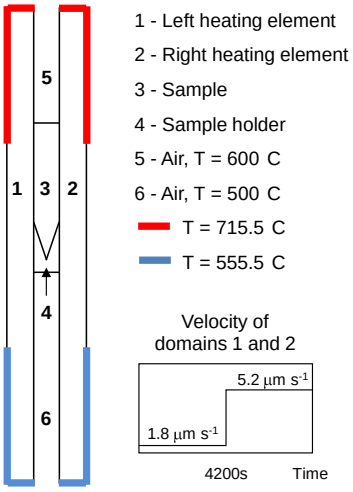

Figure 2. Simple representative geometry of the experimental device used for the numerical simulations. Domains 1 and 2 are pulled upward with a velocity profile shown in the graph, while domains 3 and 4 are fixed.

3.2. Adjustment of thermal parameters

A simple two-dimensional geometry was used (figure 2). Two heating elements, labeled 1 and 2, surround the sample and its holder, labeled 3 and 4 respectively. The thermal properties of the heating elements were defined to act as good heat conductors and the sample holder has the same thermal conductivity and heat capacity as the alloy (table 1). Cooling of the sample is provoked by translation of the heating elements with an adjusted time evolution of the velocity also shown in figure 2. Note that in the experiment, the sample and its holder are translated instead of the heating elements of the Bridgman furnace. This change is of no importance with respect to the simulation results. The size of the mushy zone is defined as the distance between the eutectic front and the highest dendrite tip position of the solidification front; it can be directly measured in the radiographs. Because the Bridgman furnace does not provide a constant imposed temperature gradient, the boundary conditions

had to be adjusted at the top and bottom regions of the heating elements in order to retrieve the time evolution of the recorded mushy zone length. Their temperatures were maintained constant, equal to 555.5°C in the cold zone and 715.5°C in the hot zone, at surfaces highlighted in bold in figure 2. Heat transfer coefficients were also imposed at the bottom of the sample holder and top of the sample i.e. at boundaries in contact with the air. Values are reported in table 1. All other boundaries are simplified assuming either a perfect contact or adiabatic conditions. It is to be noticed that, due to the relative movement of the heating elements with respect to the sample and its holder, boundary conditions are not fixed in space and need to be recalculated during the time stepping algorithms to solve the average conservation equations.

Figure 3 shows the result of the heat flow adjustment on the predicted time evolution of the position of the dendritic growth front, y_d, and the eutectic growth front, y_e, as well as on the mushy zone height, y_d-y_e. They are compared with experimental measurements. Although adjustment is not perfectly achieved, the results show that the overall kinetics of the growth front is well reproduced, as well as the increase with time of the mushy zone length. The last effect is directly linked to the gradual decrease of the temperature gradient following the mushy zone development, a phenomenon that is well known in directional solidification [15].

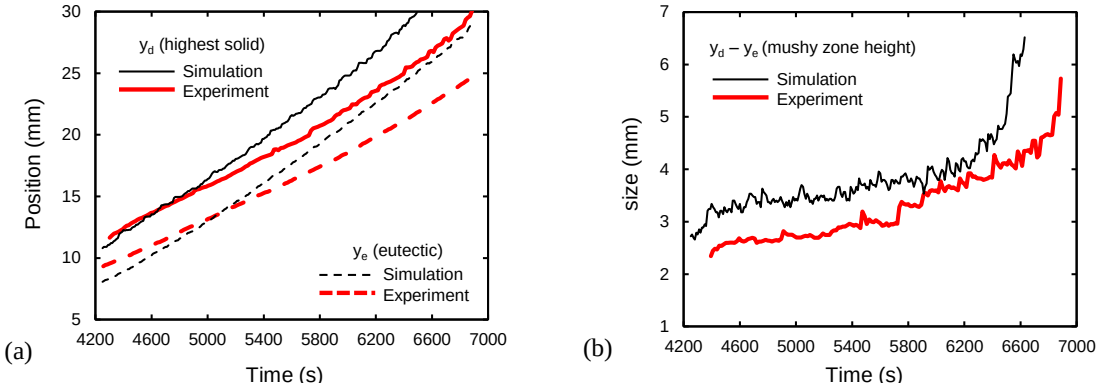

Figure 3. Measured and calculated evolutions of (a) the dendritic, y_d, and eutectic, y_e, growth fronts and (b) the mushy zone height, y_d-y_e, after increase of the pulling velocity (cf. figure 4a).

4. Results

4.1. Convective flow pattern during solidification

Even when solidification of an alloy is performed upward in stable conditions with respect to thermosolutal convection, a strong macroscopic deformation of the solidification front could be observed, initiated by the presence of a residual transverse temperature gradient and gradually amplified by solutal convection [16-18]. The occurrence of solute segregation by fluid flow is usually confirmed indirectly by observation of the solidification front (figure 4a), with a growing solid localized in the center of the sample and surrounded by eutectic after complete solidification (steepling phenomena). The convective flow pattern predicted by the numerical model is shown in figure 4c with white arrows representing the calculated fluid flow velocity field. This pattern is similar to the one previously calculated by Zhou et al. [19]. It is composed of two rolls located in the bulk liquid, on top of two other rolls located ahead of the solidifying front and penetrating into the mushy zone (figure 4d). This configuration is found to propagate upward following the progress of solidification process until the mushy zone reaches the end of the sample. Then only one roll on the left and one roll on the right remain, which disappear after complete solidification. As shown in figure 4d, the deformation of the solidification front is due to the two bottom convective rolls leading to solute accumulation on the sides of the sample. The steepling phenomenon observed experimentally is thus well reproduced and clearly visible in the simulated grain structure figure 4b. The maximum liquid velocity calculated in this region is 12 $\mu m.s^{-1}$. As expected [19] this fluid flow velocity value is larger than the actual growth

rate of 6 µm.s-1 and lower than experimental value of growth velocity for which convection becomes negligible, i.e. 20 µm.s^{-1} in previous experiments performed at ESRF with the same device [20]. It is also visible in figure 4d that liquid flow is prevalent at grain boundaries, where the solid fraction is less due to solute accumulation.

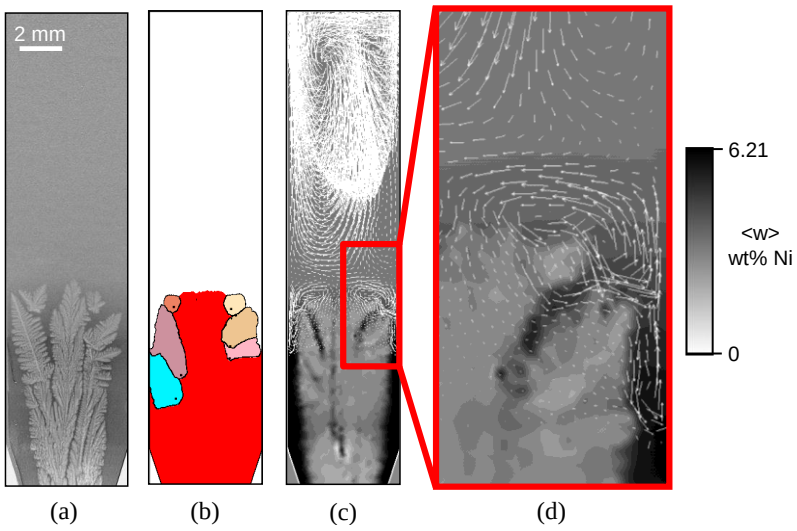

Figure 4. (a) Radiograph of the solidification front, (b) calculated grain structure and (c) composition map and fluid flow velocity field after 5200 s of pulling; the maximum velocity value in the image is approximately 135 µm s^{-1}. (d) Zoom showing the fluid flow velocity field near the solidification front in more details; the maximum velocity value in the image is approximately 12 µm s^{-1}

4.2. Eutectic fraction distribution and grain structure

The radiograph contrast is mainly linked to X-ray absorption by the chemical elements. A direct comparison can thus be made between radiography of the fully solidified sample (figure 5a) and the simulated final eutectic fraction (figure 5b) due to the fact that the eutectic fraction is also directly proportional to the local solute enrichment, i.e. to macrosegregation.

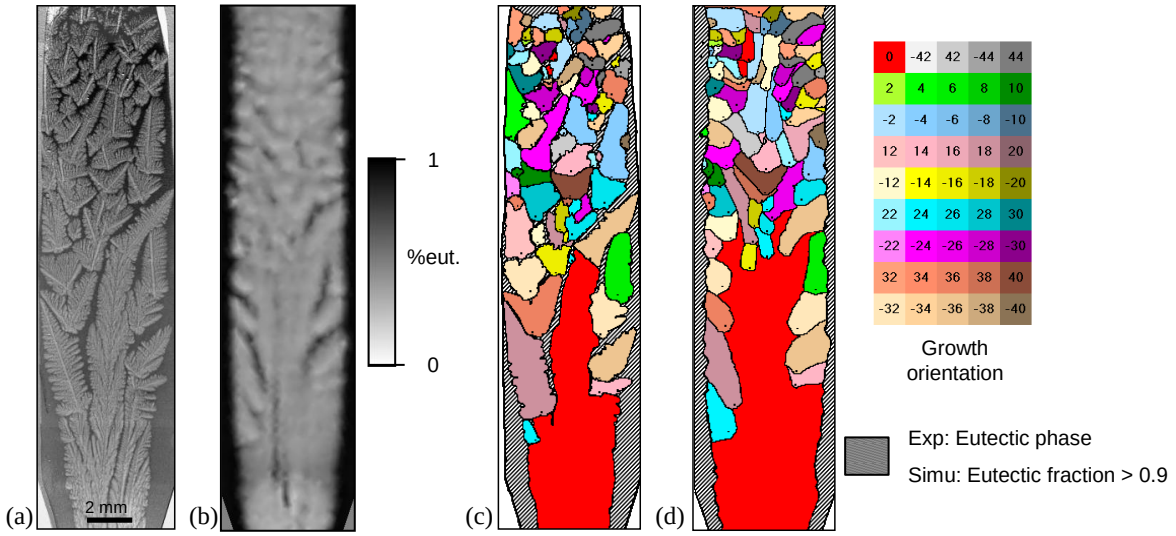

Figure 5. (a) Image of the fully solidified sample after image processing, (b) simulated final eutectic fraction, (c) experimental and (d) simulated final grain structures (color available online); the black dot in each grain indicates the position of the nucleation centre.

The distribution of inter and intragranular eutectic is partly distinguished in the simulation and similar to the experiment. Qualitatively, a higher fraction of eutectic is predicted in between the grains, as well as on the sides of the sample that correspond to the eutectic layer surrounding the grain structure observed experimentally. The last effect is made more visible in figure 5d where zones with a eutectic fraction > 0.9 are superimposed to the simulated grain structure. In the experimental images,

eutectic area are clearly visible in between the grains (figure 5a and 5c), whereas this feature is not retrieved in the numerical simulation (figure 5d). This is due to the facts that (i) direct tracking of the primary eutectic structure is not included and (ii) the FE mesh size is too coarse to reproduce this observation. Finally, comparison between figures 5c and 5d also shows that the transition from a columnar to an equiaxed grain structure is remarkably well reproduced in the simulations, with the initial columnar grain blocked at the same altitude than in the experiment. Differences between experiment and simulation in grain structure in the equiaxed zone can be mainly attributed to the fact that the nucleation positions used for the simulation were chosen as the positions of the nucleation centers in the grains after sedimentation in the experiment. This choice thus leads to a different competition between the grains during their development.

5. Conclusion

A Bridgman experiment with a refined Al - 3.5 wt% Ni alloy has been thoroughly characterized by means of X-ray radiography and provides inputs for a 2D CAFE simulation. Direct simulation of the dendritic grain structure and the eutectic distribution in the entire sample accounting for fluid flow and its interaction with the growing solid has been successfully performed. Macroscopic deformation of the solidification front by convection is well reproduced, with accumulation of solute on the sides leading to a dendrite steepling phenomenon. Distribution of eutectic fraction is qualitatively retrieved and similar position for the columnar-to-equiaxed transition is obtained. The present investigation clearly reveals the interest of coupled experimental and numerical analyses in order to get a better understanding of the physical phenomena occurring during solidification processes.

Work is currently in progress to perform further analyses by comparing experimental results with numerical simulations with and without convection for getting a more precise understanding of the effect of liquid flow on macrosegregation and grain structure. The effect of nucleation undercooling will also be investigated. Simulations using 3D multiple structure tracking in CAFE modeling [11, 21] are envisaged in the future, for example to take into account the eutectic structure formation and growth.

Acknowledgements

Financial support from ESA and CNES, and technical support of the ESRF ID19 staff members is greatly acknowledged. The cellular automaton model is implemented in the 2D finite element software R2Sol developed at MINES ParisTech CEMEF.

References

[1] Reinhart G, Nguyen-Thi H, Mangelick-Noël N, Billia B, Schenk T, and Baruchel J 7-10 June 2011 *3rd Int. Conf. on Advances in Solidification Processes*, Rolduc, Netherlands.
[2] Mathiesen R H, Arnberg L, Ramsokar K, Weitkamp T, Rau C and Snigirev A 2002 *Met. Mat. Trans. B* **33B** 613–23
[3] Schenk T, Nguyen-Thi H, Gastaldi J, Reinhart G, Cristiglio V, Mangelinck-Noël N, Klein H, Härtwig J, Grushko B, Billia B and Baruchel J 2005 *J. Cryst. Growth* **275** 201–08
[4] Yasuda H, Ohnak I, Kawasaki K, Sugiyama A, Ohmichi T, Iwane J and Umetani K 2004 *J. Cryst. Growth* **262** 645–52
[5] Guillemot G, Gandin Ch-A and Bellet M 2007 *J. Cryst. Growth* **303** 58–68
[6] Delaleau P, Beckermann C, Mathiesen R H and Arnberg L 2010 *ISIJ int* **50** 1886–94
[7] Reinhart G, Mangelinck-Noël N, Nguyen-Thi H, Schenk T, Gastaldi J, Billia B, Pino P,Härtwig J and Baruchel J 2005 *Mat. Sci. Eng. A* **413-414** 384–88
[8] Nguyen-Thi H, Reinhart G, Mangelinck-Noël N, Jung H, Billia B, Schenk T, Gastaldi J, Härtwig J and Baruchel J 2007 *Met. Mat. Trans. A* **38A** 1458–64
[9] Abramoff M D, Magelhaes P J and Ram S J 2004 *Biophotonics International* **11** 36-42
[10] Gandin Ch-A 2010 Comptes Rendus Physique **11** 216-225
[11] Carozzani T, Digonnet H, Bellet M, Gandin Ch-A, MCWASP XIII (2012) this proceedings

[12] Liu W 2005 *Finite element modelling of segregation and thermomechanical phenomena in solidification processes* Ph. D. Thesis, Ecole Nationale Supérieure des Mines de Paris, Paris, F
[13] Mosbah S, Bellet M, Gandin Ch-A 2010 Metall Mater Trans **41A** 651
[14] Gandin Ch-A, Guillemot G, Appolaire B, Niane N T 2003 Mater. Sci. & Eng **A342** 44-50
[15] Dantzig J A, Rappaz M 2009 *Solidification* (Lausanne : EPFL Press) p 457
[16] Burden M H, Hebditch D J and Hunt J D 1973 *J. Cryst. Growth* **20** 121-24
[17] Nguyen Thi H, Dabo Y, Drevet B, Dupouy M D, Camel D,Billia B, Hunt J D and Chilton A 2005 *J. Cryst. Growth* **281** 654-68
[18] Bogno A, Nguyen-Thi H, Buffet A, Reinhart G, Billia B, Mangelinck-Noël N, Bergeon N, Baruchel J and Schenk T 2011 *Acta Mater.* **59** 4356-65
[19] Zhou B H, Jung H, Mangelinck-Noël N, Nguyen-Thi H, Billia B, Liu Q S and Lan W 2008 Adv. Space Res. **41** 2112-17
[20] Reinhart G 2006 *Dynamique de formation de la microstructure de solidification d'alliages métalliques: caractérisation par imagerie X synchrotron* Ph. D. Thesis, Université Paul Cézanne Aix-Marseille III, Marseille, F
[21] Carozzani T, Digonnet H, Gandin Ch-A, Modelling Simul. Mater. Sci. Eng. **20** (2012) 015010

Table 1. Values of thermo-physical data of the Al-3.5wt%Ni alloy and numerical parameters.

Parameter	Variable	Value	Unit
Nominal composition	w_0	3.5	wt%
Liquidus temperature	T_L	650	°C
Segregation coefficient	K	0.08	wt% / wt%
Liquidus slope	m_L	-3.1	wt% $°C^{-1}$
Eutectic temperature	T_E	641.6	°C
Gibbs-Thomson coefficient	Γ	$2.41 \cdot 10^{-7}$	°C m
Heat capacity	C_p	$2.85 \cdot 10^{-6}$	J kg^{-1} $°C^{-1}$
Enthalpy of fusion	$\Delta_s^l H_f$	$9.8 \cdot 10^{-8}$	J kg^{-1}
Diffusion of Ni in liquid Al	D^l	$2.2 \cdot 10^{-9}$	m^2 s^{-1}
Dynamic viscosity	μ^l	$6 \cdot 10^{-3}$	Pa s
Solutal expansion coefficient	β_w	$-8.4 \cdot 10^{-3}$	$wt\%^{-1}$
Thermal expansion coefficient	β_T	$0.11 \cdot 10^{-3}$	$°C^{-1}$
Density	ρ_0	2450	kg m^{-3}
Thermal conductivity in the solid	κ^s	200	W m^{-1} $°C^{-1}$
Thermal conductivity in the liquid	κ^l	100	W m^{-1} $°C^{-1}$
Secondary dendrite arm spacing	λ_2	$150 \cdot 10^{-6}$	m
Primary nucleation undercooling	ΔT_n	0	°C
Location of nucleation event		Experimental input	
Cell size		$15 \cdot 10^{-6}$	m
Imposed minimum FE mesh size		$150 \cdot 10^{-6}$	m
Imposed maximum FE mesh size		$1000 \cdot 10^{-6}$	m
Objective relative error on <w>		$1 \cdot 10^{-4}$	wt%
Time step		1	s
Initial temperature		715.5	°C
Heat transfer coefficients			
Sample holder / heating elements		Perfect contact	
Sample / heating elements		Perfect contact	
Sample / sample holder		Perfect contact	
Sample / air		2000	W m^{-2} $°C^{-1}$
Sample holder / air		3000	W m^{-2} $°C^{-1}$
Heating elements / air		Adiabatic	W m^{-2} $°C^{-1}$